

---

# Explicit Boundary Guided Semi-Push-Pull Contrastive Learning for Better Anomaly Detection

---

Xincheng Yao, Chongyang Zhang\*, Ruoqi Li  
 Shanghai Jiao Tong University  
 {i-Dover, sunny\_zhang, nilponi}@sjtu.edu.cn

## Abstract

Most of anomaly detection algorithms are mainly focused on modeling the distribution of normal samples and treating anomalies as outliers. However, the discriminative performance of the model may be insufficient due to the lack of knowledge about anomalies. Thus, anomalies should be exploited as possible. However, utilizing a few known anomalies during training may cause another issue that model may be biased by those known anomalies and fail to generalize to unseen anomalies. In this paper, we aim to exploit a few existing anomalies with a carefully designed explicit boundary guided semi-push-pull learning strategy, which can enhance discriminability while mitigating bias problem caused by insufficient known anomalies. Our model is based on two core designs: First, finding one explicit separating boundary as the guidance for further contrastive learning. Specifically, we employ normalizing flow to learn normal feature distribution, then find an explicit separating boundary close to the distribution edge. The obtained explicit and compact separating boundary only relies on the normal feature distribution, thus the bias problem caused by a few known anomalies can be mitigated. Second, learning more discriminative features under the guidance of the explicit separating boundary. A boundary guided semi-push-pull loss is developed to only pull the normal features together while pushing the abnormal features apart from the separating boundary beyond a certain margin region. In this way, our model can form a more explicit and discriminative decision boundary to achieve better results for known and also unseen anomalies, while also maintaining high training efficiency. Furthermore, to make the feature learning more efficient, we propose RandAugmented CutPaste which can simulate anomalies by creating local irregularities in normal samples to mitigate the insufficient of anomaly samples. Extensive experiments on the widely-used MVTecAD benchmark show that the proposed method achieves new state-of-the-art results, with the performance of 98.8% image-level AUROC and 99.4% pixel-level AUROC.

## 1 Introduction

Anomaly detection has received widespread attention in diverse domains, such as industrial defect inspection [1–4] and medical lesion detection [5, 6]. Most of previous anomaly detection methods [7–18, 3, 19, 20, 4, 2, 21] are unsupervised and pay much attention to normal samples while overlooking the anomalies, because it is difficult to collect all kinds of anomalies. However, learning only from normal samples may cause the discriminative performance of the model to be insufficient. Without efficient discriminability, the detector’s generalization ability will be limited, and a lot of false negatives and false positives can be induced, especially for those unseen anomalies. As illustrated in Figure1(a), without anomalies, the decision boundaries are generally implicit and are

---

\*Corresponding Author. Correspondence to: Chongyang Zhang<sunny\_zhang@sjtu.edu.cn>

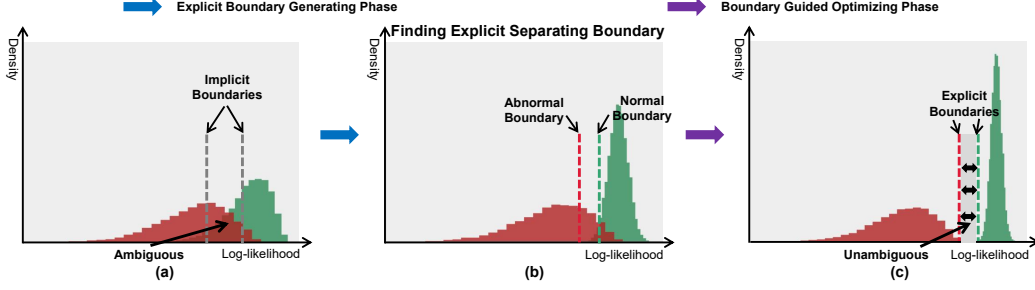


Figure 1: Conceptual illustration of our method. (a) The ambiguous anomaly score distribution with implicit decision boundaries, the boundaries are far from the ideal decision boundary. The left boundary will cause many false negatives, and the right boundary will cause many false positives. (b) The normalized normal feature distribution, and we can find explicit boundaries close to the normal distribution. (c) The unambiguous anomaly score distribution guided by explicit separating boundaries.

not discriminative enough. The *insufficient discriminability* issue is a common issue in unsupervised anomaly detection due to the lack of knowledge about anomalies. To address this issue, anomalies should be exploited as possible, fortunately, a few labeled anomalies are usually available in real-world applications.

Recently, methods which can be called semi-supervised AD [22, 23] or AD with outlier exposure [24, 25] begin to focus on those available anomalies. These methods attempt to learn knowledge from anomalies by one-class classification with anomalies as negative samples [22, 23] or by supervised binary classification [24, 25]. They show a fact that the detection performance can be improved significantly even with a few anomalies. However, the known anomalies can't represent all kinds of anomalies. These methods may be biased by the known anomalies and fail to generalize to unseen anomalies. Thus, our purpose in this paper is to learn a more discriminative anomaly detection model by exploiting a few anomalies effectively with the objective to improve detection performance on known anomalies and generalize well to unseen anomalies.

To achieve the above objective, we propose a novel and more discriminative anomaly detection model: **Boundary Guided Anomaly Detection with a Few Abnormal Samples**, termed as **BGAD-FAS**. Our model has two core designs as illustrated in Figure 1: explicit boundary generating and boundary guided optimizing.

- **Explicit Boundary Generating.** We first employ normalizing flow to learn normalized normal feature distribution (see Figure 1(b)), and obtain an explicit separating boundary close to the distribution edge. The obtained explicit and compact separating boundary only relies on the normal distribution and has no relation with the abnormal samples, thus the bias problem caused by insufficient known anomalies can be mitigated. The detailed description is in sec 3.1 and 3.2.

- **Boundary Guided Optimizing.** After obtaining the explicit separating boundary, we then propose a boundary guided semi-push-pull (BG-SPP) loss to exploit anomalies for learning more discriminative features. With the BG-SPP loss, only normal features whose log-likelihoods are smaller than the boundary are pulled together to form a more compact normal feature distribution (semi-pull); while abnormal features whose log-likelihoods are larger than the boundary are pushed apart from the boundary (semi-push). The detailed description is in sec 3.3.

In this way, our model can form a more explicit and discriminative separating boundary and also a reliable margin region for distinguishing anomalies more effectively (see Figure 1(c)). Furthermore, rarity is a critical problem of anomalies and may cause feature learning inefficient. We thus propose RandAugmented CutPaste, which can simulate anomalies by creating local irregularities in normal samples, to tackle the rarity challenge.

In summary, the main contributions of this work are three-fold:

1. We propose a novel anomaly detection model termed as BGAD-FAS, in which an explicit separating boundary is found to guide the further discriminative feature learning.

2. To exploit a few existing anomalies effectively, we propose a BG-SPP loss to pull together normal features while pushing abnormal features apart from the separating boundary, thus more discriminative features can be learned.
3. We achieve new state-of-the-art results on the widely-used MVTecAD benchmark, with the performance of 98.8% image-level AUROC and 99.4% pixel-level AUROC.

## 2 Overview and Notations

Different from the general unsupervised anomaly detection setting, the training set in this paper is composed of normal images and a few existing anomalies, denoted as  $\mathcal{I}_{train} = \mathcal{I}_n \cup \mathcal{I}_a$ , where  $\mathcal{I}_n = \{I_i\}_{i=1}^{N_0}$  and  $\mathcal{I}_a = \{I_j\}_{j=1}^{M_0}$  indicate the collection of normal samples and abnormal samples, respectively.

Figure 2 overviews our proposed method. The model consists of four parts: Feature Extractor  $f : \mathcal{I} \rightarrow \mathcal{X}$ , Conditional Normalizing Flow (CNFlow)  $\varphi_\theta : \mathcal{X} \rightarrow \mathcal{Z}$ , Explicit Boundary Generating and Boundary Guided Optimizing. We refer the features extracted by the feature extractor as input features for CNFlow, and denote these features as  $\mathcal{X} = \mathcal{X}_n \cup \mathcal{X}_a$ , where  $\mathcal{X}_n = \{x_i\}_{i=1}^N$  and  $\mathcal{X}_a = \{x_j\}_{j=1}^M$  are normal and abnormal features, respectively. The training procedure can be divided into two phases as shown in Figure 2: explicit boundary generating and boundary guided optimizing. In the testing procedure, the CNFlow can assign corresponding log-likelihoods for input features, and the log-likelihoods can be converted to anomaly scores (see Anomaly Scoring in sec3.2). We denote our **Boundary Guided Anomaly Detection** model without and with a **Few Abnormal Samples** as **BGAD** and **BGAD-FAS**, respectively.

## 3 Our Proposed Method

### 3.1 Learning Normal Feature Distribution by Normalizing Flow

In order to find one anomaly-independent separating boundary, one normalized distribution of normal features should be learned firstly. Normalizing flow is employed to learn normal feature distribution in our method.

**Conditional Normalizing Flow.** Formally, we denote  $\varphi_\theta : \mathcal{X} \in \mathbb{R}^d \rightarrow \mathcal{Z} \in \mathbb{R}^d$  as our normalizing flow. It is built as a composition of coupling layers [26] such that  $\varphi_\theta = \varphi_L \circ \dots \circ \varphi_2 \circ \varphi_1$ , where  $\theta$  is the trainable parameters and  $L$  is the total number of layers. Defining  $d$ -dimensional input and output features of normalizing flow as  $y_0 = x \in \mathcal{X}$  and  $y_L = z \in \mathcal{Z}$ , the latents can be computed as  $y_l = \varphi_l(y_{l-1})$ , where  $\{y_l\}_{l=1}^{L-1}$  are the intermediate outputs. The input distribution estimated by model  $p_\theta(x)$  can be calculated according to the change of variables formula as follows [26][27]:

$$\log p_\theta(x) = \log p_\mathcal{Z}(\varphi_\theta(x)) + \sum_{l=1}^L \log |\det J_{\varphi_l}(y_{l-1})| \quad (1)$$

where  $J_{\varphi_l}(y_{l-1}) = \frac{\partial \varphi_l(y_{l-1})}{\partial y_{l-1}}$  is the Jacobian matrix of the transformation  $\varphi_l$  at  $y_{l-1}$ . Normalizing flow can approximate the feature distribution  $p_\mathcal{X}$  with  $p_\theta(x)$ . The set of parameters  $\theta$  is obtained by optimizing the log-likelihoods across the training distribution  $p_\mathcal{X}$ :

$$\theta^* = \underset{\theta \in \Theta}{\operatorname{argmin}} \mathbb{E}_{x \sim p_\mathcal{X}} [-\log p_\theta(x)] \quad (2)$$

The coupling layers in normalizing flow are generally implemented by fully connected layers, so the spatial position relationship will be destroyed because the 2D feature maps are flattened to 1D. To preserve the positional information, we add 2D-aware position embeddings to the feature maps [28].

**Normalizing Normal Feature Distribution.** We then employ normalizing flow to learn normal feature distribution by maximum likelihood optimization. The latent variable distribution  $p_\mathcal{Z}(z)$ ,  $z \in \mathbb{R}^d$  can generally be assumed to obey the multivariate Gaussian distribution [28, 29] as follows:

$$p_\mathcal{Z}(z) = (2\pi)^{-\frac{d}{2}} \det(\Sigma)^{-\frac{1}{2}} e^{-\frac{1}{2}(z-\mu)^T \Sigma^{-1} (z-\mu)} \quad (3)$$

When training normal features, the latent variables for normal features can be assumed to obey  $\mathcal{N}(0, \mathbf{I})$  for further simplicity. By replacing  $p_\mathcal{Z}(z) = (2\pi)^{-\frac{d}{2}} e^{-\frac{1}{2}z^T z}$  in formula1, the optimization

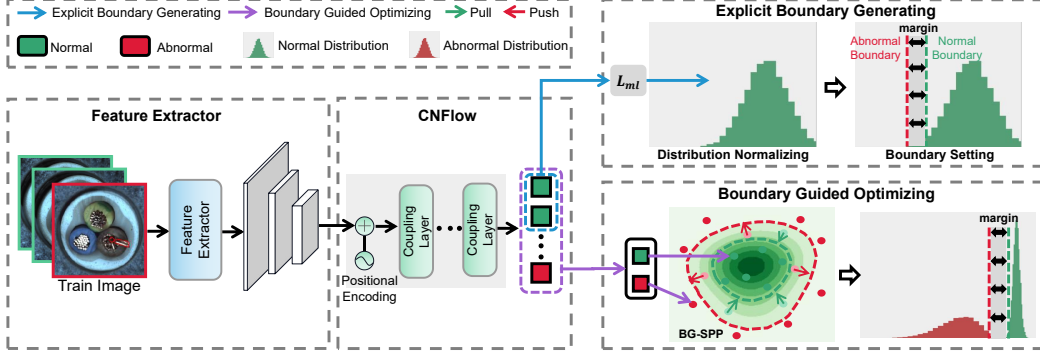


Figure 2: Overview of our model. The extracted feature maps are transformed into a latent space using a conditional normalizing flow (CNFlow), which is then used to generate an anomaly score for each input feature. The training procedure can be divided into two phases: explicit boundary generating and boundary guided optimizing. In the first phase, only normal samples and ML loss (Eq.5) are utilized for model training to obtain a relatively stable normal log-likelihood distribution, and then one explicit separating boundary can be obtained based on the learned distribution. In the second phase, with the explicit boundary and the BG-SPP loss (Eq.8), both normal and abnormal samples are utilized for model training, so as to learn more discriminative features.

objective in the formula 2 can be rewritten as:

$$\theta^* = \underset{\theta \in \Theta}{\operatorname{argmin}} \mathbb{E}_{x \sim p_{\mathcal{X}}} \left[ \frac{1}{2} \varphi_{\theta}(x)^T \varphi_{\theta}(x) - \sum_{l=1}^L \log |\det J_{\varphi_l}(y_{l-1})| + \frac{d}{2} \log(2\pi) \right] \quad (4)$$

The maximum likelihood loss function for optimizing normal features can be defined as:

$$\mathcal{L}_{ml} = \mathbb{E}_{x \in \mathcal{X}_n} \left[ \frac{1}{2} \varphi_{\theta}(x)^T \varphi_{\theta}(x) - \sum_{l=1}^L \log |\det J_{\varphi_l}(y_{l-1})| + \frac{d}{2} \log(2\pi) \right] \quad (5)$$

### 3.2 Finding an Explicit and Compact Separating Boundary

With the learned normal distribution, one explicit and compact separating boundary can be found, and then be used as the guidance for further contrastive learning.

**Anomaly Scoring.** The advantage of normalizing flow is that we can estimate the exact log-likelihood for each input feature  $x$  as follows:

$$\log p(x) = -\frac{1}{2} \varphi_{\theta}(x)^T \varphi_{\theta}(x) + \sum_{l=1}^L \log |\det J_{\varphi_l}(y_{l-1})| - \frac{d}{2} \log(2\pi) \quad (6)$$

where the  $\log p(x)$  means the log-likelihood of  $x$ . With the estimated log-likelihood, we can convert it to likelihood via the exponential function. As we maximize log-likelihoods for normal features in Eq.(5), the likelihood can directly measure the normality. Thus, we can generate the anomaly score by using maximum likelihood to subtract each likelihood value as follows:

$$s(x) = \max_{x' \in \mathcal{X}} (\exp(\log p(x'))) - \exp(\log p(x)) \quad (7)$$

where the  $s(x)$  means the anomaly score of  $x$ . Because the exponential function is monotonic, the log-likelihood can be equivalently converted to the anomaly score. Thus, the separating boundary in log-likelihood distribution is equivalent to the separating boundary in anomaly score distribution.

**Finding Explicit Separating Boundaries.** We then obtain separating boundaries based on log-likelihood distribution. We build the boundaries through the following two steps:

**1. Building normal log-likelihood distribution.** We can employ log-likelihood estimation formulation in Eq.(6) to obtain all log-likelihoods of normal features  $\mathcal{P}_n = \{\log p_i\}_{i=1}^N$ . The  $\mathcal{P}_n$  can be used to approximate log-likelihood distribution of all normal features.

**2. Finding explicit normal and abnormal boundary.** Considering normal features are relatively sufficient, the closer the separating boundary is to the normal log-likelihood distribution, the more



conducive it is to distinguish the anomalies. However, if we set the boundary too close to the distribution center, the samples in the tail of the normal distribution are more likely to be misclassified as abnormal. Thus, we define a position hyperparameter  $\beta$  to control the distance from the boundary to the center. We select the  $\beta$ -th percentile (*i.e.*  $\beta = 5$ ) of sorted normal log-likelihood distribution as the normal boundary  $b_n$ , which also indicates the upper bound of the normal false positive rate is  $\beta\%$ . To make the feature learning more robust, we further introduce a margin hyperparameter  $\tau$  and define an abnormal boundary  $b_a = b_n - \tau$ . The boundaries are shown in Figure 2.

The obtained explicit and compact (close to the normal distribution edge) separating boundary only relies on the normal distribution and has no relation with the abnormal samples, thus our method can avoid the bias problem caused by insufficient known anomalies (as validated in sec 4.3).

### 3.3 Learning More Discriminative Features by Boundary Guided Semi-Push-Pull

With the explicit normal and abnormal boundary, we propose a boundary guided semi-push-pull (BG-SPP) loss for more discriminative feature learning. Our BG-SPP loss can utilize the boundary  $b_n$  as the contrastive object (boundary guided), and only pull together normal features whose log-likelihoods are smaller than  $b_n$  (semi-pull) while pushing abnormal features whose log-likelihoods are larger than  $b_a$  apart from  $b_n$  at least beyond the margin  $\tau$  (semi-push). The formulation of the BG-SPP loss is defined as:

$$\begin{aligned}\mathcal{L}_{bg-spp}^0 &= \|\min((\mathcal{P}_n - \mathcal{B}_n), 0)\|_0 + \|\max((\mathcal{P}_a - \mathcal{B}_n + \mathcal{T}), 0)\|_0 \\ &= \|\min((\mathcal{P}_n - \mathcal{B}_n), 0)\|_0 + \|\max((\mathcal{P}_a - \mathcal{B}_a), 0)\|_0\end{aligned}\quad (8)$$

where  $\mathcal{B}_n = b_n \cdot \mathbf{1}_N$  and  $\mathcal{B}_a = \mathcal{B}_n - \mathcal{T} = (b_n - \tau) \cdot \mathbf{1}_M$  are boundary parameters. We define BG-SPP loss as  $\ell_0$  norm based formulation to encourage the sparse log-likelihood distribution in the margin region  $(b_a, b_n)$ , because any log-likelihood  $\log p_i$  fallen into the margin region  $(b_a, b_n)$  will increase the value of  $\mathcal{L}_{bg-spp}^0$ . Since the log-likelihoods can range from  $(-\infty, 0]$ , the large region makes it difficult to select the margin hyperparameter  $\tau$ . Thus, we define a large enough normalizer  $\alpha_n = -\alpha \cdot b_n$  (*i.e.*  $\alpha = 5$ ) and employ it to normalize the log-likelihoods to the range  $[-1, 0]$ . We also denote that the extremely small log-likelihoods can be excluded outside the BG-SPP loss in Eq. 8, as these log-likelihoods can be easily divided into anomalies. Therefore, minimizing the BG-SPP loss will encourage all log-likelihoods  $\mathcal{P}$  to distribute in the regions  $[-1, b_a]$  or  $[b_n, 0]$ . Even without anomalies, our model can also be optimized by the first part of the BG-SPP loss. In the second training phase, the objective function is as follows:

$$\mathcal{L} = \mathcal{L}_{ml} + \lambda \mathcal{L}_{bg-spp}^0 \quad (9)$$

Minimizing the objective function in Eq. (9) is a classical  $\ell_0$  norm optimization problem which is usually non-continuous and non-convex. For the original  $\ell_0$  norm based formulation, we have that  $\min((\mathcal{P}_n - \mathcal{B}_n), 0) \in [-1, 0]^N$  and  $\max((\mathcal{P}_a - \mathcal{B}_a), 0) \in [0, 1]^M$ . As the  $\ell_1$  norm is a convex envelope of  $\ell_0$  norm in the unit hypercube  $[-1, 1]^{N+M}$ , we can convert the  $\ell_0$  norm based form to the  $\ell_1$  norm based form for easier optimization:

$$\mathcal{L}_{bg-spp}^1 = \sum_{i=1}^N |\min((\log p_i - b_n), 0)| + \sum_{j=1}^M |\max((\log p_j - b_n + \tau), 0)| \quad (10)$$

We further provide an error bound analysis for the learning objective in Appendix A.4.

### 3.4 RandAugmented CutPaste

In this subsection, we propose RandAugmented CutPaste (RACP), which can simulate anomalies by randomly creating local irregularities, to improve the quantity as well as the diversity of irregular patterns. The whole procedure is illustrated in Appendix A.5 and summarized as follows:

1. Adapted from RandAugment [30], we first select  $K$  available image transformations and probabilities of applying each transformation to construct an augmentation set  $\mathcal{T} := \{T_1, \dots, T_K | T_k : \mathcal{I} \rightarrow \mathcal{I}\}$ : {AutoContrast, Equalize, Rotate, Posterize, Solarize, Brightness, Sharpness, Translate, Shear}.
2. Randomly selecting an augmentation subset  $T_{RS} \sim \mathcal{T}$  containing  $S$  transformations to augment an abnormal sample:  $I'_a = T_{RS}(I_a), I_a \in \mathcal{I}_a$ .

Table 1: Image-level anomaly detection and pixel-level anomaly localization results on the MVTecAD dataset.  $\cdot/\cdot$  means pixel-level AUROC and PRO. The results of our model are averaged over three independent runs.

|                  | Category   | AD w/o Abnormal Samples |            |            |               |             |             |             | AD w/ Abnormal Samples |         |  |
|------------------|------------|-------------------------|------------|------------|---------------|-------------|-------------|-------------|------------------------|---------|--|
|                  |            | SPADE [4]               | DFR [35]   | P-SVDD [3] | CutPaste [36] | PaDiM [2]   | MSFD [37]   | BGAD (Ours) | FCDD [18]              | DRA [6] | BGAD-FAS (Ours)                                      |
| Textures         | Carpet     | 0.975/0.947             | 0.970/0.93 | 0.926/-    | 0.983/-       | 0.991/0.962 | 0.990/0.958 | 0.994/0.981 | 0.99/-                 | -/-     | <b>0.997</b> $\pm$ 0.0002/ <b>0.991</b> $\pm$ 0.0004 |
|                  | Grid       | 0.937/0.867             | 0.980/0.93 | 0.962/-    | 0.975/-       | 0.973/0.946 | 0.986/0.937 | 0.994/0.975 | 0.95/-                 | -/-     | <b>0.997</b> $\pm$ 0.0002/ <b>0.988</b> $\pm$ 0.0001 |
|                  | Leather    | 0.976/0.972             | 0.980/0.97 | 0.974/-    | 0.995/-       | 0.992/0.978 | 0.978/0.924 | 0.997/0.993 | 0.99/-                 | -/-     | <b>0.998</b> $\pm$ 0.0001/ <b>0.994</b> $\pm$ 0.0003 |
|                  | Tile       | 0.874/0.759             | 0.870/0.79 | 0.914/-    | 0.905/-       | 0.941/0.860 | 0.952/0.841 | 0.969/0.929 | 0.98/-                 | -/-     | <b>0.994</b> $\pm$ 0.0077/ <b>0.978</b> $\pm$ 0.0021 |
|                  | Wood       | 0.874/0.885             | 0.830/0.91 | 0.908/-    | 0.955/-       | 0.949/0.911 | 0.953/0.925 | 0.970/0.956 | 0.94/-                 | -/-     | <b>0.986</b> $\pm$ 0.0053/ <b>0.977</b> $\pm$ 0.0007 |
| Objects          | Bottle     | 0.984/0.955             | 0.970/0.93 | 0.981/-    | 0.976/-       | 0.983/0.948 | 0.985/0.940 | 0.989/0.960 | 0.96/-                 | -/-     | <b>0.994</b> $\pm$ 0.0009/ <b>0.976</b> $\pm$ 0.0011 |
|                  | Cable      | 0.972/0.909             | 0.920/0.81 | 0.968/-    | 0.900/-       | 0.967/0.888 | 0.972/0.922 | 0.978/0.969 | 0.93/-                 | -/-     | <b>0.992</b> $\pm$ 0.0010/ <b>0.999</b> $\pm$ 0.0030 |
|                  | Capsule    | 0.990/0.937             | 0.990/0.96 | 0.958/-    | 0.974/-       | 0.990/0.935 | 0.979/0.878 | 0.990/0.945 | 0.95/-                 | -/-     | <b>0.992</b> $\pm$ 0.0021/ <b>0.965</b> $\pm$ 0.0033 |
|                  | Hazelnut   | 0.991/0.954             | 0.990/0.97 | 0.975/-    | 0.973/-       | 0.991/0.926 | 0.982/0.968 | 0.985/0.977 | 0.97/-                 | -/-     | <b>0.994</b> $\pm$ 0.0040/ <b>0.981</b> $\pm$ 0.0028 |
|                  | Metal nut  | 0.981/0.944             | 0.930/0.90 | 0.980/-    | 0.931/-       | 0.981/0.856 | 0.972/0.985 | 0.974/0.950 | 0.98/-                 | -/-     | <b>0.996</b> $\pm$ 0.0003/ <b>0.972</b> $\pm$ 0.0012 |
|                  | Pill       | 0.965/0.946             | 0.970/0.96 | 0.951/-    | 0.957/-       | 0.914/0.927 | 0.971/0.929 | 0.982/0.979 | 0.99/-                 | -/-     | <b>0.997</b> $\pm$ 0.0003/ <b>0.986</b> $\pm$ 0.0005 |
|                  | Screw      | 0.989/0.960             | 0.990/0.96 | 0.957/-    | 0.967/-       | 0.989/0.944 | 0.983/0.924 | 0.990/0.952 | 0.93/-                 | -/-     | <b>0.992</b> $\pm$ 0.0003/ <b>0.966</b> $\pm$ 0.0010 |
|                  | Toothbrush | 0.979/0.935             | 0.990/0.93 | 0.981/-    | 0.981/-       | 0.979/0.931 | 0.986/0.877 | 0.984/0.935 | 0.95/-                 | -/-     | <b>0.992</b> $\pm$ 0.0003/ <b>0.949</b> $\pm$ 0.0026 |
|                  | Transistor | 0.941/0.874             | 0.840/0.79 | 0.970/-    | 0.930/-       | 0.941/0.845 | 0.886/0.781 | 0.936/0.845 | 0.90/-                 | -/-     | <b>0.992</b> $\pm$ 0.0005/ <b>0.982</b> $\pm$ 0.0015 |
|                  | Zipper     | 0.965/0.926             | 0.960/0.90 | 0.951/-    | 0.993/-       | 0.965/0.959 | 0.981/0.935 | 0.987/0.951 | 0.98/-                 | -/-     | <b>0.995</b> $\pm$ 0.0003/ <b>0.975</b> $\pm$ 0.0002 |
| Mean             |            | 0.960/0.917             | 0.950/0.91 | 0.957/-    | 0.960/-       | 0.975/0.921 | 0.970/0.915 | 0.981/0.953 | 0.96/-                 | -/-     | <b>0.994</b> $\pm$ 0.0007/ <b>0.979</b> $\pm$ 0.0006 |
| Image-level Mean |            | 0.835                   | 0.938      | 0.921      | 0.971         | 0.979       | 0.964       | 0.968       | -                      | 0.959   | <b>0.988</b> $\pm$ 0.0012                            |

3. Cutting the anomalous regions of the augmented abnormal sample:  $\mathcal{R}_a = \text{Cut}(I'_a)$ .

4. Pasting the cropped anomalous regions back to a random normal sample at a random location:  $I''_a = \text{Paste}(I_n, \mathcal{R}_a)$ ,  $I_n \in \mathcal{I}_n$ .

RACP can mitigate the rarity problem at the image level, we further propose Asymmetric Focal Weighting for the objective function to focus on hard normal features and abnormal features at the loss level. Details and effectiveness of these methods are provided in Appendix A.5.

## 4 Experiments

### 4.1 Datasets and Metrics

**Datasets.** In this work, we focus on anomalies in real-world applications, such as industrial defect inspection and medical lesion detection. Thus, anomaly datasets with natural anomalies are evaluated in our experiments rather than the semantic anomaly datasets used in many previous studies under the one-vs-all protocols. Specifically, we evaluate six real-world anomaly detection datasets, including four industrial defect inspection datasets: **MVTecAD** [1], **BTAD** [31], **AITEX** [32] and **ELPV** [33]; and two medical image datasets for detecting lesions on different organs: **BrainMRI** [5] and **HeadCT** [5]. A more detailed introduction of these datasets is provided in Appendix A.2.

**Evaluation Metrics.** The performance of BGAD-FAS and all comparable methods are evaluated by the area under the curve (AUC) of the receiver operating characteristic (ROC) at the image or pixel level (AUROC). In order to weight ground-truth anomaly regions of various sizes equally, we also adopt the Per-Region-Overlap (PRO) curve metric proposed in [34].

The implementation details can be found in Appendix A.3. The BGAD-FAS is trained with five anomaly samples per category by default if not specified.

### 4.2 Comparison with the State-of-the-Art

**MVTecAD.** We compare our BGAD-FAS with the state-of-the-art anomaly detection methods, including SPADE [4], DFR [35], P-SVDD [3], PaDiM [2], CutPaste [36], MSFD [37] under the metrics of image-level AUROC, pixel-level AUROC and PRO (Table 1). The detailed pixel-level AUROC, and PRO comparison results of all categories are shown in Table 1. As shown in Table 1, the BGAD can achieve comparable results with the SOTA methods while the BGAD-FAS reaches the best performance under all three evaluation metrics. Our BGAD-FAS can further surpass unsupervised BGAD by 2.0%, 1.3% and 2.6% for image-level AUROC, pixel-level AUROC, and PRO, respectively. What’s more, the largest gain in PRO demonstrates that the proposed method is not only effective in anomaly detection but also in anomaly localization to better locate the anomalous area.

**BTAD.** We compare our BGAD-FAS with three baseline methods reported in [31]: AutoEncoder with MSE loss, AutoEncoder with SSIM loss, and VT-ADL. In [31], only pixel-level AUROCs are reported, thus we also only evaluate anomaly localization performance under metrics of pixel-level AUROC and PRO. The detailed pixel-

Table 2: Pixel-level anomaly localization results measured by pixel-wise AUROC on BTAD dataset. All the other results are from [31].  $\cdot/\cdot$  means pixel-level AUROC and PRO. The results of our model are averaged over three independent runs.

| Categories | AE MSE [38] | AE SSIM [14] | VT-ADL [31]  | BGAD (Ours) | BGAD-FAS (Ours)                                      |
|------------|-------------|--------------|--------------|-------------|--|
| 1          | 0.490       | 0.530        | <b>0.990</b> | 0.972/0.767 | 0.980 $\pm$ 0.0027/ <b>0.797</b> $\pm$ 0.0318        |
| 2          | 0.920       | 0.960        | 0.940        | 0.967/0.578 | <b>0.977</b> $\pm$ 0.0018/ <b>0.623</b> $\pm$ 0.0173 |
| 3          | 0.950       | 0.890        | 0.770        | 0.996/0.988 | <b>0.998</b> $\pm$ 0.0003/ <b>0.993</b> $\pm$ 0.0005 |
| Mean       | 0.780       | 0.790        | 0.900        | 0.978/0.778 | <b>0.985</b> $\pm$ 0.0015/ <b>0.804</b> $\pm$ 0.0163 |

Table 3: Image-level anomaly detection results on the AITEX, ELPV, BrainMRI, and HeadCT datasets. All reported image-level AUROCs are averaged over three independent runs. All the other results are from [6].

| Dataset  | AD w/o Abnormal Samples<br>KDAD [5] | AD w/ Abnormal Samples |             |             |             |                     |                     |
|----------|-------------------------------------|------------------------|-------------|-------------|-------------|---------------------|---------------------|
|          |                                     | DevNet [39]            | FLOS [40]   | SAOE [41]   | MLEP [42]   | DRA [6]             | BGAD-FAS (Ours)     |
| AITEX    | 0.576±0.002                         | 0.598±0.070            | 0.538±0.073 | 0.675±0.094 | 0.564±0.055 | 0.692±0.124         | <b>0.826</b> ±0.011 |
| ELPV     | 0.744±0.001                         | 0.514±0.076            | 0.457±0.056 | 0.635±0.092 | 0.578±0.062 | 0.675±0.024         | <b>0.903</b> ±0.003 |
| BrainMRI | 0.733±0.016                         | 0.694±0.004            | 0.693±0.036 | 0.531±0.060 | 0.632±0.017 | <b>0.744</b> ±0.004 | 0.740±0.006         |
| HeadCT   | 0.598±0.070                         | 0.742±0.076            | 0.698±0.092 | 0.597±0.022 | 0.758±0.038 | 0.796±0.105         | <b>0.807</b> ±0.004 |

level AUROC and PRO comparison results of all categories are shown in

Table 2. Our BGAD-FAS can achieve 98.5% mean pixel-level AUROC which surpasses other methods as high as 8.5% AUROC, and surpasses unsupervised BGAD by 0.7%. What’s more, BGAD-FAS can achieve 80.4% PRO which surpasses unsupervised BGAD by 2.6%.

**Other Datasets.** For the other datasets, we compare our BGAD-FAS with six recent and closely related SOTA methods reported in [6]: unsupervised KDAD [37], and open-set supervised DevNet [39], FLOS [40], SAOE [41], MLEP [42] and DRA [6]. In [6], only image-level AUROCs are reported, thus we also only evaluate anomaly detection performance under the metric of image-level AUROC. Similar to the setting in [6], all models are trained with one anomaly sample. The image-level anomaly detection results are shown in Table3. Our model can achieve the best AUROC performance on the two industrial defect inspection datasets (AITEX and ELPV), and comparable results with the SOTA methods on the two medical lesion detection datasets (BrainMRI and HeadCT). Specifically, our model surpasses the previous SOTA method DRA by 13.4% and 22.8% on the AITEX and ELPV datasets respectively. These results combined with the results of MVTEC-AD and BTAD datasets demonstrate that our method is more suitable for the industrial defect inspection tasks. The detection results on diverse datasets across application domains also demonstrate our method’s generalization ability in different applications.

### 4.3 Ablation Study

**Experiments On Hard Subsets From MVTEC-AD.** MVTEC-AD dataset contains many easy anomalies, and the detection performance on these anomalies is hard to be improved further. Thus, results obtained on the full MVTEC-AD dataset can’t fully demonstrate the effectiveness of our model. In order to thoroughly verify the effectiveness of our method, we further construct two more difficult subsets from the MVTEC-AD dataset. The details of subset selection are provided in AppendixA.7. The first subset is used to verify our model’s anomaly detection performance, and the second subset is used to verify our model’s anomaly localization performance. The results are shown in Table 5. It can be found that the detection and localization performance gain on these hard subsets is larger than that on the original dataset with a margin of 1.0%, 1.3%, and 6.0% respectively. This ablation study demonstrates that our model is more beneficial for harder anomaly categories.

**Boundary Hyperparameters.** To verify the influence of normal boundary (controlled by  $\beta$ ) and abnormal boundary (controlled by  $\tau$ ) on the model’s detection performance, we evaluate different combinations of  $\beta$  (1%, 5%, 10%) and  $\tau$  (0.1, 0.2, 0.3). Experimental results are shown in Table 4. From Table 4, we can draw the following main conclusions: 1)  $\beta$  has a more significant effect on performance compared with  $\tau$ , and pixel-wise AUROC is insensitive to the hyperparameters. 2) Our model is insensitive to the margin  $\tau$ , which means our model can achieve superior results as long as a certain margin is formed between normal and abnormal. 3) Better detection results can be obtained by decreasing the  $\beta$ . Generally, a lower  $\beta$  means the normal boundary is closer to the distribution edge, thus the results show that the closer the separating boundary is to the normal log-likelihood distribution edge, the more conducive it is to distinguish the anomalies. The best results can be achieved with the combination of  $\beta = 1\%$  and  $\tau = 0.1$  among all combinations.

Table 4: Anomaly detection and localization results on MVTEC-AD dataset according to hyperparameter  $\beta$  and  $\tau$ .  $\cdot / \cdot / \cdot$  means mean image-level AUROC, mean pixel-level AUROC and mean PRO.

| $\beta \backslash \tau$ | 0.1                          | 0.2                           | 0.3                  |
|-------------------------|------------------------------|-------------------------------|----------------------|
| 1%                      | <b>0.9916</b> /0.9940/0.9779 | 0.9915/0.9940/0.9782          | 0.9906/0.9938/0.9778 |
| 5%                      | 0.9896/0.9942/0.9789         | 0.9898/ <b>0.9943</b> /0.9793 | 0.9902/0.9941/0.9792 |
| 10%                     | 0.9877/0.9942/0.9789         | 0.9900/0.9942/ <b>0.9794</b>  | 0.9905/0.9942/0.9792 |

Table 5: Anomaly detection and localization results on subsets from the MVTecAD dataset. Image AUROC is measured on the first subset. Pixel AUROC and PRO are measured on the second subset. see details in AppendixA.7.

| Metric \ Dataset | MVTecAD |              | Hard Subsets |              | Unseen Subsets |              |
|------------------|---------|--------------|--------------|--------------|----------------|--------------|
|                  | BGAD    | BGAD-FAS     | BGAD         | BGAD-FAS     | BGAD           | BGAD-FAS     |
| Image AUROC      | 0.968   | 0.988(+2.0%) | 0.948        | 0.978(+3.0%) | 0.948          | 0.971(+2.3%) |
| Pixel AUROC      | 0.981   | 0.994(+1.3%) | 0.960        | 0.986(+2.6%) | 0.960          | 0.982(+2.2%) |
| PRO              | 0.953   | 0.979(+2.6%) | 0.863        | 0.949(+8.6%) | 0.863          | 0.930(+6.7%) |

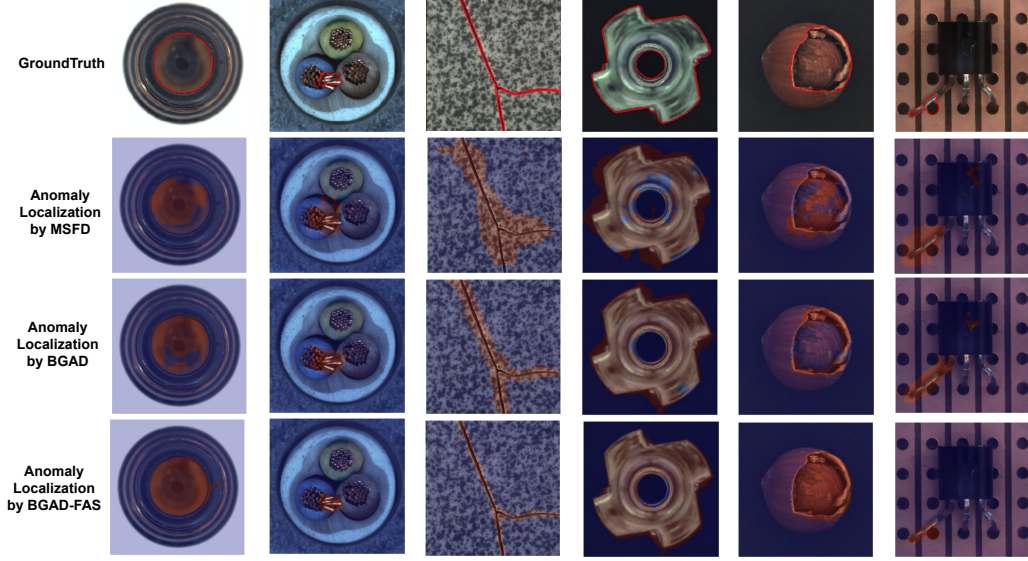


Figure 4: Qualitative results. The anomaly localization results generated by MSFD [37], BGAD, and BGAD-FAS are shown for comparison. In the first row, the areas enclosed by the red lines are ground-truth. In the other rows, areas marked by red are generated anomaly localization results.

**Generalization Capability and Learning Efficiency.** In order to verify the generalization capability to unseen anomalies, we only select a subset of anomalies to participate in training. We use the easy subsets as the training set and validate results on the hard subsets to explore the generalization capability of the model. The easy subsets are formed by excluding the hard subsets mentioned above from the original dataset. The experiment results are shown in Table 5. It can be found that even only trained with easy anomalies, the model can generalize well to hard anomalies with performance gain by 2.3%, 2.2%, and 6.7% for image-level AUROC, pixel-level AUROC, and PRO respectively. The detect results illustrate the generalization capability to unseen anomalies of our model. To illustrate the learning efficiency, we show AUROC vs epoch curve in Figure 3, specifically, the pixel-level AUROC with FAS converges rapidly compared to its counterparts. The AUROC can increase a large margin generally only a meta epoch (8 epochs) after adding BG-SPPC loss for optimization.

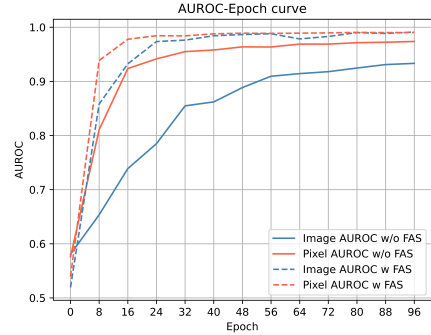


Figure 3: AUROC vs epoch curve of cable category on MVTecAD dataset.

#### 4.4 Qualitative Results

We visualize some anomaly localization results in Figure 4 with the MVTecAD dataset. It can be found that our BGAD-FAS can generate more accurate anomaly localization maps with the guidance of the explicit boundary (see columns of {1,3,4,5,6} in Figure 4), or even generate anomaly maps better than ground truth (see columns of {2} in Figure 4).

## 5 Related Work

**Unsupervised Approaches.** Most of anomaly detection methods are unsupervised and only learn from normal samples, such as AutoEncoder [13–16], GAN [9, 10, 7, 8, 11, 12] and one-class-classification (OCC) [43, 44, 17, 3] based methods. Recently, most of superior methods utilize pre-trained deep models, such as DeepKNN [20], GaussianAD [21], SPADE [4] and PaDiM [2]. There are also some anomaly detection methods based on knowledge distillation [34, 37], feature reconstruction [35], and normalizing flows [29, 28].

**Supervised Approaches.** Currently, a few existing works are similar to ours, *i.e.* AD with outlier exposure [24, 25] and deep semi-supervised AD [22, 23, 18]. In [24], Hendrycks,*et al.* term random nature images from the large scale datasets that are likely not nominal as outlier exposure, and explore how to utilize such data to improve unsupervised AD. The method presented in [25] utilizes thousands of OE samples to achieve state-of-the-art results on standard image AD benchmarks. DeepSAD [22] is the first deep model utilizing a few anomalies by generalizing the unsupervised DeepSVDD [17] method to a semi-supervised AD setting. In [23], Ruff,*et al.* further modify the DeepSAD based on cross-entropy classification that concentrates nominal samples, this modification significantly improves the performance of DeepSAD. FCDD proposed in [18] extends the pseudo-Huber loss in [23] to construct a semi-supervised anomaly localization framework. However, these methods didn’t consider the model’s bias to known anomalies. The recent work DRA [6] is the most similar to ours, which also considers the model’s generalization to unseen anomalies. The DRA model can learn disentangled representations of anomalies to enable generalized detection. Different from prior works, we aim to exploit anomalies with a carefully designed explicit boundary guided semi-push-pull strategy, which can enhance discriminability while mitigating the bias problem caused by insufficient known anomalies.

## 6 Conclusion

In this paper, we propose a novel and more discriminative anomaly detection model termed as BGAD-FAS to tackle the *insufficient discriminability* issue and the *bias* issue simultaneously. By exploiting a few anomalies effectively, our model can learn more discriminative features for distinguishing anomalies. With the explicit and compact separating boundary, our model can avoid the bias problem caused by a few known anomalies. Considering the rarity of anomalies, we further propose RandAugmented CutPaste. The experimental results show BGAD-FAS’s ability to achieve or outperform SOTA anomaly detection methods on six real-world anomaly detection datasets.

## References

- [1] P. Bergmann, M. Fauser, D. Sattlegger, and C. Steger, “Mvtec ad - a comprehensive real-world dataset for unsupervised anomaly detection,” *In CVPR*, 2019.
- [2] T. Defard, A. Setkov, A. Loesch, and R. Audigier, “Padim: a patch distribution modeling framework for anomaly detection and localization,” *In 1st International Workshop on Industrial Machine Learning*, 2021.
- [3] J. Yi and S. Yoon, “Patch svdd: Patch-level svdd for anomaly detection and segmentation,” *In Asian Conference on Computer Vision*, 2021.
- [4] N. Cohen and Y. Hoshen, “Sub-image anomaly detection with deep pyramid correspondences,” 2020, arXiv preprint arXiv: 2005.02357v3.
- [5] M. Salehi, N. Sadjadi, S. Baselizadeh, M. H. Rohban, and H. R. Rabiee, “Multiresolution knowledge distillation for anomaly detection,” *In IEEE Conference on Computer Vision and Pattern Recognition*, 2021.
- [6] C. Ding<sup>1</sup>, G. Pang, and C. Shen, “Catching both gray and black swans: open-set supervised anomaly detection,” *In CVPR*, 2022.
- [7] S. Akcay, A. Atapour-Abarghouei, and T. P. Breckon, “Ganomaly: Semi-supervised anomaly detection via adversarial training,” *In ACCV*, p. 622–637, 2018.

- [8] H. Zenati, M. Romain, C. S. Foo, B. Lecouat, and V. R. Chandrasekhar, “Adversarially learned anomaly detection,” *In ICDM*, pp. 727–736, 2018.
- [9] T. Schlegl, P. Seebock, S. M. Waldstein, U. Schmidt-Erfurth, and G. Langs, “Unsupervised anomaly detection with generative adversarial networks to guide marker discovery,” *In International Conference on Information Processing in Medical Imaging*, 2017.
- [10] T. Schlegl, P. Seebock, S. M. Waldstein, G. Langs, and U. Schmidt-Erfurth, “Fast unsupervised anomaly detection with generative adversarial networks,” *In Medical Image Analysis*, 2017.
- [11] S. Pidhorskyi, R. Almohsen, D. A. Adjeroh, and G. Doretto, “Generative probabilities novelty detection with adversarial autoencoders,” *In Conference and Workshop on Neural Information Processing Systems*, 2018.
- [12] M. Sabokrou, M. Khalooei, M. Fathy, and E. Adeli, “Adversarially learned one-class classifier for novelty detection,” *In IEEE Winter Conference on Application of Computer Vision*, 2018.
- [13] J. Chen, S. Sathe, C. Aggarwal, and D. Turaga, “Outlier detection with autoencoder ensembles,” *In SIAM International Conference on Data Mining*, pp. 90–98, 2017.
- [14] P. Bergmann, S. Lowe, M. Fauser, D. Sattlegger, and C. Steger, “Improving unsupervised defect segmentation by applying structural similarity to autoencoders,” *In International Conference on Computational Vision Technologies and Applications*, 2019.
- [15] D. T. Nguyen, Z. Lou, M. Klar, and T. Brox, “Anomaly detection with multiple-hypotheses predictions,” *In International Conference on Machine Learning*, 2019.
- [16] D. Davletshina, V. Melnychuk, V. Tran, H. Singla, M. B. adn Evgeniy Faerman, M. Fromm, and M. Schubert, “Unsupervised anomaly detection for x-ray image,” 2020, arXiv preprint arXiv:2001.10883.
- [17] L. Ruff, R. A. Vandermeulen, N. Gornitz, L. Deecke, and S. A. Siddiqui, “Deep one-class classification,” *In International Conference on Machine Learning*, 2021.
- [18] P. Liznerski, L. Ruff, R. A. Vandermeulen, B. J. Franks, M. Kloft, and K.-R. Muller, “Explainable deep one-class classification,” *In International Conference on Learning Representations*, 2021.
- [19] I. Golan and R. El-Yaniv, “Deep anomaly detection using geometric transformations,” *In Conference and Workshop on Neural Information Processing Systems*, 2018.
- [20] L. Bergman, N. Cohen, and Y. Hoshen, “Deep nearest neighbor anomaly detection,” 2020, arXiv preprint arXiv: 2002.10445.
- [21] O. Rippel, P. Mertens, and D. Merhof, “Modeling the distribution of normal data in pre-trained deep features for anomaly detection,” 2020, arXiv preprint arXiv: 2005.14140.
- [22] L. Ruff, R. A. Vandermeulen, N. Gornitz, A. Binder, E. Müller, K.-R. Müller, and M. Kloft, “Deep semi-supervised anomaly detection,” *In International Conference on Learning Representations*, 2021.
- [23] L. Ruff, R. A. Vandermeulen, B. J. Franks, K.-R. Muller, and M. Kloft, “Rethinking assumptions in deep anomaly detection,” 2020, arXiv preprint arXiv:2006.00339.
- [24] D. Hendrycks, M. Mazeika, and T. Dietterich, “Deep anomaly detection with outlier exposure,” *In International Conference on Learning Representations*, 2019.
- [25] D. Hendrycks, M. Mazeika, S. Kadavath, and D. Song, “Using self-supervised learning can improve model robustness and uncertainty,” *In Conference and Workshop on Neural Information Processing Systems*, 2019.
- [26] L. Dinh, D. Krueger, and Y. Bengio, “Nice: Non-linear independent components estimation,” *In International Conference on Learning Representations*, 2015.

- [27] L. Dinh, J. Sohl-Dickstein, and S. Bengio, “Density estimation using real nvp,” *In International Conference on Learning Representations*, 2017.
- [28] D. Gudovskiy, S. Ishizaka, and K. Kozuka, “Cflow-ad: Real-time unsupervised anomaly detection with localization via conditional normalizing flows,” *In IEEE Winter Conference on Application of Computer Vision*, 2022.
- [29] M. Rudolph, B. Wandt, and B. Rosenhahn, “Same same but different: Semi-supervised defect detection with normalizing flows,” *In IEEE Winter Conference on Application of Computer Vision*, 2021.
- [30] E. D. Cubuk, B. Zoph, J. Shlens, and Q. V. Le, “RandAugment: Practical automated data augmentation with a reduced search space,” *In CVPR*, 2020.
- [31] P. Mishra, R. Verk, D. Fornasier, C. Piciarelli, and G. L. Foresti, “Vt-adl: A vision transformer network for image anomaly detection and localization,” 2021, arXiv preprint arXiv:2104.10036.
- [32] J. Silvestre-Blanes<sup>1</sup>, T. Alberio-Alberio<sup>1</sup>, I. Miralles, R. Pérez-Llorens, and J. Moreno, “A public fabric database for defect detection methods and results,” *In Autex Research Journal*, 2019.
- [33] S. Deitscha, V. Christlein, S. Berger, C. Buerhop-Lutz, A. Maier, F. Gallwitz, and C. Riess, “Automatic classification of defective photovoltaic module cells in electroluminescence images,” *In Solar Energy*, pp. 455–468, 2019.
- [34] P. Bergmann, M. Fauser, D. Sattlegger, and C. Steger, “Uninformed students: Student-teacher anomaly detection with discriminative latent embeddings,” *In CVPR*, 2020.
- [35] J. Yang, Y. Shi, and Z. Qi, “Dfr: Deep feature reconstruction for unsupervised anomaly segmentation,” 2020, arXiv preprint arXiv: 2012.0712.
- [36] C.-L. Li, K. Sohn, J. Yoon, and T. Pfister, “Cutpaste: Self-supervised learning for anomaly detection and localization,” *In CVPR*, 2021.
- [37] G. Wang, S. Han, E. Ding, and D. Huang, “Student-teacher feature pyramid matching for unsupervised anomaly detection,” *In British Machine Vision Conference*, 2021.
- [38] G. E. Hinton and R. R. Salakhutdinov, “Reducing the dimensionality of data with neural networks,” *In Science* 313, 5786, 2006.
- [39] G. Pang, C. Ding, C. Shen, and A. van den Hengel, “Explainable deep few-shot anomaly detection with deviation networks,” 2021, arXiv preprint arXiv:2108.00462.
- [40] T.-Y. Lin, P. Goyal, R. Girshick, K. He, and P. Dollar, “Focal loss for dense object detection,” *In ICCV*, 2017.
- [41] J. Tack, S. Mo, J. Jeong, and J. Shin<sup>†</sup>, “Csi: Novelty detection via contrastive learning on distributionally shifted instances,” *In Conference and Workshop on Neural Information Processing Systems*, 2020.
- [42] W. Liu, W. Luo, Z. Li, P. Zhao, and S. Gao<sup>1</sup>, “Margin learning embedding prediction for video anomaly detection with a few anomalies,” *In International Joint Conference on Artificial Intelligence*, 2019.
- [43] B. Schölkopf, J. C. Platt, J. Shawe-Taylor, A. J. Smola, and R. C. Williamson, “Estimating the support of a high-dimensional distribution,” *In Neural Computation*, p. 1443–1471, 2001.
- [44] D. M. TAX and R. P. DUIN, “Support vector data description,” *In Machine Learning*, pp. 45–66, 2004.
- [45] M. Tan and Q. V. Le, “Efficientnet: Rethinking model scaling for convolutional neural networks,” *In International Conference on Machine Learning*, 2019.
- [46] H. Zenati, M. Romain, C. S. Foo, B. Lecouat, and V. R. Chandrasekhar, “Pytorch image models,” 2019, <https://github.com/rwightman/pytorch-image-models>.

- [47] L. Ardizzone, C. Lüth, J. Kruse, C. Rother, and U. Köthe, “Guided image generation with conditional invertible neural networks,” 2019, arXiv preprint arXiv: 1907.02392.
- [48] D. P. Kingma and P. Dhariwal, “Glow: Generative flow with invertible 1x1 convolutions,” *In Conference and Workshop on Neural Information Processing Systems*, 2019.
- [49] J.-H. Jacobsen, A. Smeulders, and E. Oyallon, “i-revnet: Deep invertible networks,” *In International Conference on Learning Representations*, 2018.
- [50] S. Chen, G. Niu, C. Gong, J. Li, J. Yang, and M. S. . 3, “Large-margin contrastive learning with distance polarization regularizer,” *In International Conference on Machine Learning*, 2017.

## Checklist

1. For all authors...
  - (a) Do the main claims made in the abstract and introduction accurately reflect the paper’s contributions and scope? [\[Yes\]](#) See Section 3.
  - (b) Did you describe the limitations of your work? [\[Yes\]](#) See Section A.1.
  - (c) Did you discuss any potential negative societal impacts of your work? [\[No\]](#) We currently haven’t considered the possible negative societal impacts of our work.
  - (d) Have you read the ethics review guidelines and ensured that your paper conforms to them? [\[Yes\]](#)
2. If you are including theoretical results...
  - (a) Did you state the full set of assumptions of all theoretical results? [\[N/A\]](#)
  - (b) Did you include complete proofs of all theoretical results? [\[N/A\]](#)
3. If you ran experiments...
  - (a) Did you include the code, data, and instructions needed to reproduce the main experimental results (either in the supplemental material or as a URL)? [\[Yes\]](#) But the code will be released after paper acceptance.
  - (b) Did you specify all the training details (e.g., data splits, hyperparameters, how they were chosen)? [\[Yes\]](#) See Appendix A.3, A.5 and A.4.
  - (c) Did you report error bars (e.g., with respect to the random seed after running experiments multiple times)? [\[Yes\]](#) See Table 1, 2, and 3
  - (d) Did you include the total amount of compute and the type of resources used (e.g., type of GPUs, internal cluster, or cloud provider)? [\[Yes\]](#) See Appendix A.3.
4. If you are using existing assets (e.g., code, data, models) or curating/releasing new assets...
  - (a) If your work uses existing assets, did you cite the creators? [\[Yes\]](#) See Appendix A.3.
  - (b) Did you mention the license of the assets? [\[Yes\]](#) See Appendix A.3.
  - (c) Did you include any new assets either in the supplemental material or as a URL? [\[Yes\]](#) The code will be released after paper acceptance.
  - (d) Did you discuss whether and how consent was obtained from people whose data you’re using/curating? [\[No\]](#)
  - (e) Did you discuss whether the data you are using/curating contains personally identifiable information or offensive content? [\[No\]](#)
5. If you used crowdsourcing or conducted research with human subjects...
  - (a) Did you include the full text of instructions given to participants and screenshots, if applicable? [\[N/A\]](#)
  - (b) Did you describe any potential participant risks, with links to Institutional Review Board (IRB) approvals, if applicable? [\[N/A\]](#)
  - (c) Did you include the estimated hourly wage paid to participants and the total amount spent on participant compensation? [\[N/A\]](#)



## A Appendix

### A.1 Limitations

In this paper, we propose a novel and more discriminative anomaly detection model termed as BGAD-FAS to tackle the *insufficient discriminability* issue and the *bias* issue simultaneously. Our core insight is to set an explicit separating boundary to guide the further discriminative feature learning. We thus employ normalizing flow to obtain an explicit separating boundary due to its exact log-likelihood estimation ability. However, not all anomaly detection models can generate log-likelihoods, thus our method can't be used in these models directly. But we are also able to implement our *explicit separating boundary* insight in these methods in other ways and then improve these models. Another limitation is that our method requires anomalous samples to achieve better results, but it is difficult to collect all kinds of anomalies. Thus, generalization performance to unseen anomalies is a critical problem that we should consider, the experimental results in sec4.3 validate our model's generalization capability. Therefore, future work includes further improving the model's generalization capability to unseen anomalies, tackling the imbalance between normal and abnormal more effectively.

### A.2 Dataset Details

**MVTecAD.** The MVTec Anomaly Detection dataset [1] contains 5354 high-resolution images (3629 images for training and 1725 images for testing) of 15 different categories. 5 classes consist of textures and the other 10 classes contain objects. A total of 73 different defect types are presented and almost 1900 defective regions are manually annotated in this dataset.

**BTAD.** The BeanTech Anomaly Detection dataset [31] contains 2830 real-world images of 3 industrial products. Product 1, 2, and 3 of this dataset contain 400, 1000, and 399 training images respectively.

**AITEX.** The AITEX [32] is a fabric defect inspection dataset that has 12 defect categories. The original images in this dataset are  $4096 \times 256$  resolution, we convert this dataset to MVTecAD format following the converting method used in the work [6].

**ELPV.** The ELPV [33] dataset contains 2642 samples of  $300 \times 300$  resolution. The dataset is used for solar cell defect inspection and contains two defect categories: mono- and poly-crystalline.

**BrainMRI.** The BrainMRI is a brain tumor detection dataset obtained by magnetic resonance imaging (MRI) of the brain. The dataset can be downloaded from the Kaggle competition <https://www.kaggle.com/datasets/navoneel/brain-mri-images-for-brain-tumor-detection>.

**HeadCT.** The HeadCT is a head hemorrhage detection dataset obtained by a CT scan of the head. The dataset can be downloaded from the Kaggle competition <https://www.kaggle.com/datasets/felipekitamura/head-ct-hemorrhage>.

### A.3 Implementation Details

As illustrated in Figure 2, we use Efficient-b6 [45] pre-trained on ImageNet [46] dataset as feature extractor to extract three levels of feature maps with  $\{4\times, 8\times, 16\times\}$  downsampling ratios. The parameters of the feature extractor are frozen in the training process. The extracted multi-scale features are then transformed to latent space by the normalizing flow, the normalizing flow is constructed by 8 coupling layers similar to [28]. We train BGAD-FAS and unsupervised BGAD using Adam optimizer with  $2e-4$  learning rate, 200 train epochs, 32 mini-batch size, and cosine learning rate annealing strategy with 2 warm-up epochs. The normalizer described in sec3.3 is set to 10 by default, the hyperparameter  $\lambda$  in E.q.9 is set to 1.0 by default, the default number of transformations in augmentation subset is set as 3. All the training and test images are resized and cropped to  $256 \times 256$  resolution from the original resolution. Our main code is based on the CFLOW implementation made public by the authors of [28] under the MIT license. The pre-trained feature extractor Efficient-b6 is from the timm [46] library under the Apache 2.0 license.

The normalizing flow in our model is mainly based on Real-NVP [27] architecture, but the convolutional subnetwork in Real-NVP is replaced with a linear subnetwork. Our CNFlow also combines many design efforts of various works on normalizing flows from recent works [47–49]. As in previous works, the normalizing flow in our model is composed of the so-called *coupling layers*.

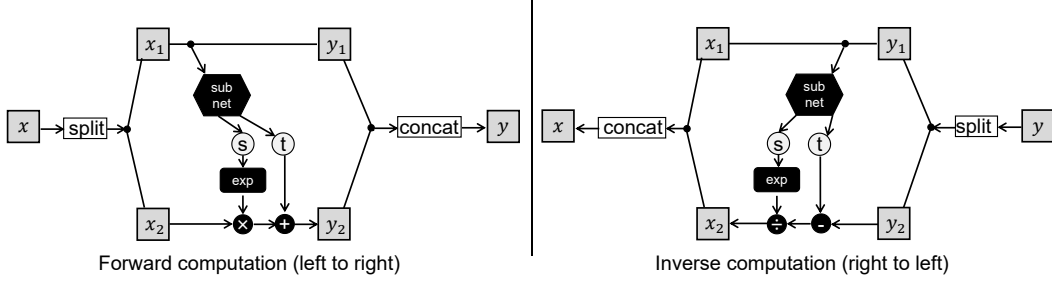


Figure 5: Illustration of a coupling layer. The transformation coefficients are predicted by a subnetwork (*subnet*), which is composed of fully-connected layers, nonlinear activations, batch normalization layers, *etc.*. The forward affine coupling can be calculated as  $y_1 = x_1; y_2 = x_2 \odot \exp(s(x_1)) + t(x_1)$ , and the inverse affine coupling is then calculated as  $x_1 = y_1; x_2 = (y_2 - t(y_1))/\exp(s(y_1))$ .

In our CNFlow, each coupling layer is designed to achieve the forward or inverse affine coupling computation [27] as illustrated in Figure 5. And the native coupling layer is followed by random and fixed soft permutation of channels [47], and a fixed scaling by a constant, similar to ActNorm layers introduced by [48]. For the coupling coefficients, each subnetwork predicts multiplicative and additive components jointly, as done by [48]. Furthermore, we adopt the soft clamping of multiplication coefficients used by [27]. The implementation of the normalizing flow in our model is based on the FrEIA library <https://github.com/VLL-HD/FrEIA>, thanks to the authors’ contributions, we can implement non-trivial normalizing flow conveniently.

The total parameters of our model are 43M. Our model can be trained by one GPU card, the memory usage of our model is only about 2600MB, which means that training our model generally doesn’t appear out-of-memory issue. In experiments, we train the model on the MVTecAD dataset with one Titan-XP GPU card, the total training time is about 30 hours, and the inference speed of our model is about 16fps achieved by Titan-XP.

#### A.4 Error Bound Analysis

**Proposition 1.** Assume that  $\varphi_{\theta^*} \in \operatorname{argmin}_{\varphi_{\theta}, \theta \in \Theta} \{\mathcal{L}_{ml} + \lambda \mathcal{L}_{bg-spp}^1\}$ , and  $y = 0, y = 1$  means normal and abnormal features. Then we have that

$$\begin{aligned} & \mathbb{E}_{y_i=0}[\max((b'_n - \log p_i), 0)] + \mathbb{E}_{y_j=1}[\max((\log p_j - b'_a), 0)] \\ & \leq (b_n - b_a) \mathcal{L}_{bg-spp}^1(\varphi_{\theta^*}) + N/(N+M)[\max(1+b'_n, -b'_a)] \\ & \leq \frac{(\frac{d}{2} \log(2\pi) - \frac{1}{2})(b_n - b_a)}{\lambda} + N/(N+M) \end{aligned} \quad (11)$$

where the  $b'_n = b_n - \epsilon, b'_a = b_a + \epsilon, \epsilon \in (0, b_n - b_a)$ ,  $N$  and  $M$  are the number of normal and abnormal features.

*proof.* The derivation procedure mainly follows the Theorem 3 in [50]. We denote that  $\log p_1 \geq \log p_2 \geq \dots \geq \log p_{N+M}$  is a ranking of the log likelihoods, where  $N$  and  $M$  are the number of normal and abnormal log likelihoods respectively. Then for  $b_n = \log p_N$ , we have that

$$\begin{aligned} & \mathbb{E}_{y_i=0}[\max((b'_n - \log p_i), 0)] + \mathbb{E}_{y_j=1}[\max((\log p_j - b'_a), 0)] \\ & \leq (b'_n - b'_a) \mathcal{L}_{bg-spp}^0(\varphi_{\theta^*}) + N/(N+M)[\max(1+b'_n, -b'_a)] \\ & \leq (b_n - b_a) \mathcal{L}_{bg-spp}^1(\varphi_{\theta^*}) + N/(N+M) \end{aligned} \quad (12)$$

The first inequality is obtained by assuming the worst case where  $\log p_1, \dots, \log p_N$  are all misclassified and the others are fallen in  $(b_a, b_n)$ . The second inequality is obtained as  $1 + b'_n \leq 1$  and  $-b'_a \leq 1$  when  $-1 \leq b'_a < b'_n \leq 0$  satisfies.

Furthermore, for any  $\varphi_0$  satisfying  $\mathcal{L}_{bg-spp}^1(\varphi_0) = 0$ , by the optimality of  $\varphi_{\theta^*}$ , we have that

$$\mathcal{L}_{ml}(\varphi_{\theta^*}) + \lambda \mathcal{L}_{bg-spp}^1(\varphi_{\theta^*}) \leq \mathcal{L}_{ml}(\varphi_{\theta^0}) + \lambda \mathcal{L}_{bg-spp}^1(\varphi_{\theta^0}) = \mathcal{L}_{ml}(\varphi_{\theta^0}) \quad (13)$$

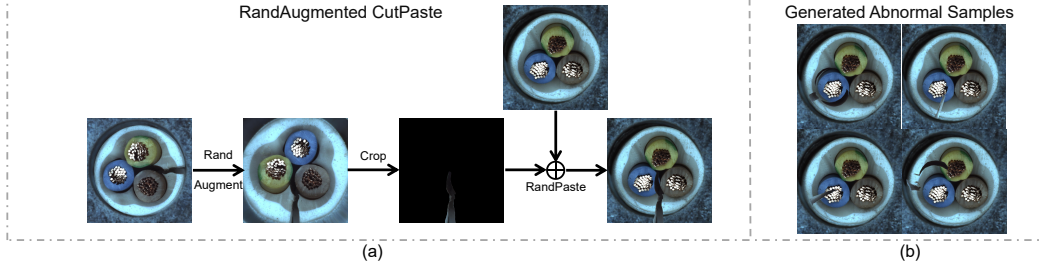


Figure 6: (a) Process to generate abnormal samples, and (b) generated abnormal samples by RandAugmented CutPaste.

and thus (the similarity function  $g$  in SPPC loss is specified as the general exponentiated-cosine distance function for simplifying derivation)

$$\begin{aligned}
& \mathcal{L}_{bg-spp}^1(\varphi_{\theta^*}) \\
& \leq (\mathcal{L}_{ml}(\varphi_{\theta^0}) - \mathcal{L}_{ml}(\varphi_{\theta^*})) / \lambda \\
& \leq \frac{1}{\lambda} \left( \frac{1}{2} \varphi_{\theta^0}(x)^T \varphi_{\theta^0}(x) - \frac{1}{2} \varphi_{\theta^*}(x)^T \varphi_{\theta^*}(x) + \frac{1}{2} \varphi_{\theta^*}(x)^T \varphi_{\theta^*}(x) + \frac{d}{2} \log(2\pi) \right) \\
& \leq \frac{1}{\lambda} \left( -\frac{1}{2} + \frac{d}{2} \log(2\pi) \right) \\
& = \frac{\frac{d}{2} \log(2\pi) - \frac{1}{2}}{\lambda}
\end{aligned} \tag{14}$$

The second inequality is obtained by assuming the worst initial states:

$$\varphi_{\theta^0}(x)^T \varphi_{\theta^0}(x) = 1 \tag{15}$$

By combining the above E.q.(12) and E.q.(14), we have that

$$\begin{aligned}
& \mathbb{E}_{y_i=0}[\max((b'_n - \log p_i), 0)] + \mathbb{E}_{y_j=1}[\max((\log p_j - b'_a), 0)] \\
& \leq \frac{(\frac{d}{2} \log(2\pi) - \frac{1}{2})(b_n - b_a)}{\lambda} + N/(N + M)
\end{aligned} \tag{16}$$

The above proposition demonstrates that the necessity and usefulness of the BG-SPP loss, because increasing the hyperparameter  $\lambda$  would assist the error bound in converging to zero. And the proposition also implies that increasing anomalies will benefit the reliability of the normal and abnormal discrimination.

#### A.5 RandAugmented CutPaste and Asymmetric Focal Weighting

The whole procedure of RandAugmented CutPaste (RACP) is illustrated in Figure 6. More generated abnormal samples by RandAugmented CutPaste are shown in Figure 7. The advantage of RACP is that learning on generated samples to recognize irregularities can generalize well on unseen anomalies. The limitation is that RACP is still not a perfect imitation of real anomalies.

We further propose Asymmetric Focal Weighting (AFW) for the objective function to focus on hard normal features and abnormal features to mitigate the rarity problem.

**Weighting for Hard Normal Features.** For easy normal features, the weights are assigned as 1. For hard normal features, higher weights should be assigned. Let  $\alpha_n$  and  $\gamma_n$  are the normal focusing parameters, we propose Truncated Focal Weighting as follows:

$$Fw_{n_i} = \begin{cases} 1.0, & \text{if } \log p_i > \log p_n; \\ -\alpha_n(1 - p_i)^{\gamma_n} \log p_i, & \text{if } \log p_i \leq \log p_n. \end{cases} \tag{17}$$

**Weighting for Abnormal Features.** Abnormal features with larger log-likelihood can be regarded as hard positives. We propose Reversed Focal Weighting to assign higher weights for abnormal

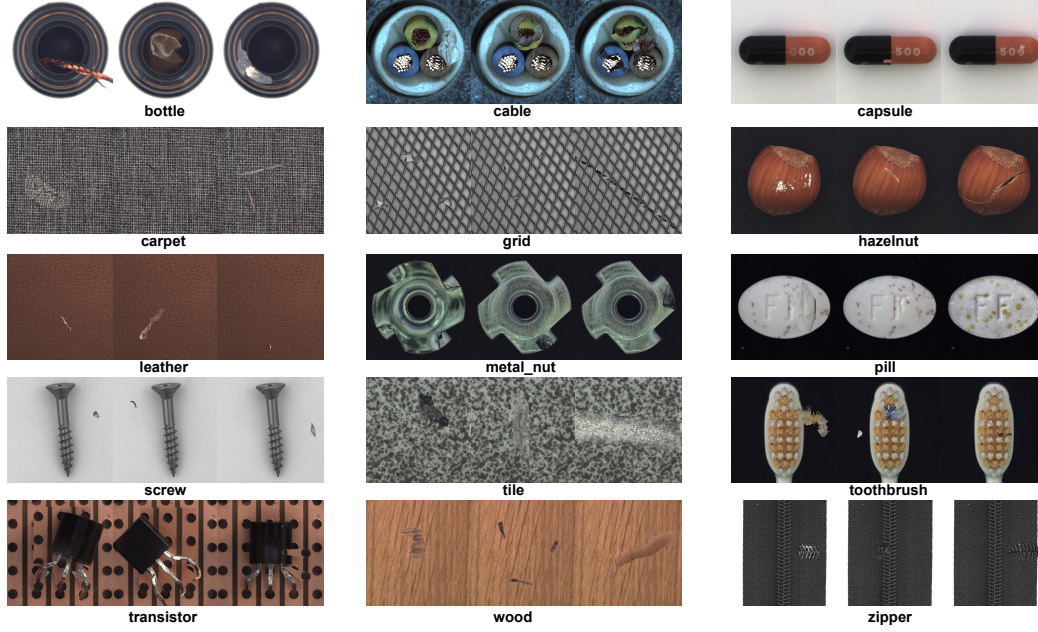


Figure 7: Generated abnormal samples by RandAugmented CutPaste. All product categories of MVTecAD dataset are shown in the Figure.

features and much higher weights for hard positives. However, the weighting factors may be less than 1 for abnormal features with smaller log-likelihoods in Reversed Focal Weighting. Therefore, we introduce a truncation term, 1 will be assigned as weights for easy abnormal features. Let  $\alpha_a$  and  $\gamma_a$  are the normal focusing parameters, the weighting formula is defined as follows:

$$Fw_{a_j} = \begin{cases} -\alpha_a(1 + p_j)^{\gamma_a} \frac{1}{\log p_j}, & \text{if } \log p_j > \log p_a; \\ 1.0, & \text{if } \log p_j \leq \log p_a. \end{cases} \quad (18)$$

**Hyperparameter Settings.** In E.q.17, we set  $\log p_n = -2$  (features with log-likelihoods larger than  $-2$  can be regarded as easy normal features empirically), and  $\alpha_n = 15, \gamma_n = 1$  to make  $Fw_{n_i}$  more smooth at  $\log p_i = -2$ . In E.q.18, we set  $\log p_a = -20$  (features with log-likelihoods less than  $-20$  can be regarded as easy abnormal features empirically), and  $\alpha_a = 0.53, \gamma_a = 2$  to make  $Fw_{a_j}$  more smooth at  $\log p_j = -20$ .

**Detailed Focal Weighted Learning Objective.** The detailed focal weighted learning objective is formulated as follows:

$$\begin{aligned} \mathcal{L} &= \mathcal{L}_{ml} \odot \mathcal{FW}_1 + \lambda \mathcal{L}_{bg-spp}^1 \odot \mathcal{FW}_2 \\ &= \mathbb{E}_{x_i \in \mathcal{X}_n} \left[ Fw_{n_i} \cdot \left( \frac{1}{2} \varphi_\theta(x)^T \varphi_\theta(x) - \sum_{l=1}^L \log |\det J_{\varphi_l}(y_{l-1})| + \frac{d}{2} \log(2\pi) \right) \right] \\ &\quad + \sum_{i=1}^{|\mathcal{X}_n|} Fw_{n_i} \cdot |\min((\log p_i - b_n), 0)| + \sum_{j=1}^{|\mathcal{X}_a|} Fw_{a_j} \cdot |\max((\log p_j - b_n + \tau), 0)| \end{aligned} \quad (19)$$

**Effect of RandAugmented CutPaste and Asymmetric Focal Weighting.** To show the effectiveness of RandAugmented CutPaste, we show experimental results with or without RandAugmented CutPaste in Table 6. It can be found that our method can effectively improve the detection performance even if only one anomaly per category is used. Under the setting of one anomaly, the results can be improved by 0.3%, 0.3%, and 1.0% for image-level AUROC, pixel-level AUROC, and PRO, respectively. Under the setting of five anomalies, the results can be improved by 0.5%, 0.3%, and 0.7% for image-level AUROC, pixel-level AUROC, and PRO, respectively. What's more, the detection and localization performance can be further improved by Asymmetric Focal Weighting.

Table 6: The ablation study on MVTecAD dataset to verify the effectiveness of RandAugmented CutPaste and Asymmetric Focal Weighting. n: n existing anomalies used in training.

| 1 | 5 | RACP | AFW | Image AUROC  | Pixel AUROC  | PRO          |
|---|---|------|-----|--------------|--------------|--------------|
|   |   |      |     | 0.968        | 0.981        | 0.953        |
| ✓ |   |      |     | 0.982        | 0.985        | 0.959        |
| ✓ |   | ✓    |     | 0.985        | 0.988        | 0.969        |
|   | ✓ |      |     | 0.983        | 0.991        | 0.969        |
|   | ✓ | ✓    |     | 0.988        | 0.994        | 0.976        |
|   | ✓ | ✓    | ✓   | <b>0.989</b> | <b>0.995</b> | <b>0.979</b> |

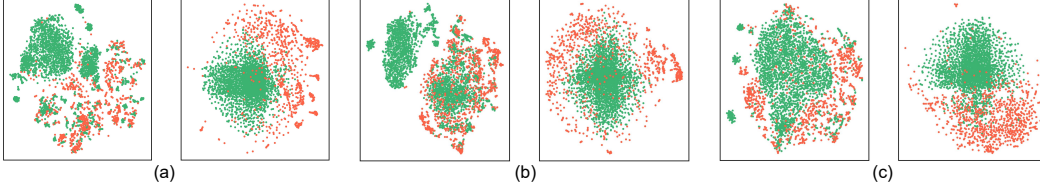


Figure 8: Feature distributions for (a) capsule category, (b) pill category and (c) screw category. Left is feature distribution w/o anomaly samples, right is feature distribution with anomaly samples.

The experimental results show that RandAugmented CutPaste and Asymmetric Focal Weighting mitigate the rarity problem effectively.

#### A.6 Feature Distribution and Log-Likelihood Histogram Visualization

To illustrate the effectiveness of our method more intuitively, we visualize normal and abnormal feature distribution and log-likelihood histogram in Figure 8,9. From Figure 8, it can be found that the difference between normal and abnormal features is more obvious in our BGAD-FAS. From Figure 9, it can be found that the ambiguous log-likelihood regions can be diminished by our BGAD-FAS.

#### A.7 Details of Hard and Unseen Subset Selection

In order to thoroughly verify the effectiveness of our method, we further construct two more difficult subsets from the MVTecAD dataset. The first subset is constructed to evaluate the detection performance, thus we select the subset based on the image-level AUROC. Specifically, we select the first subset based on the misclassification at the image level, *i.e.* anomaly categories are selected if several samples of these categories are detected as normal. The second subset is constructed to evaluate the localization performance, thus we select the subset based on the pixel-level AUROC. Specifically, anomaly categories are selected if their pixel-level AUROCs are the lowest among all anomaly categories. The constructed subsets are shown in Table7. In order to verify the generalization capability of our model, we only use the easy subsets as the training set and validate results on the hard subsets. Thus, the hard subsets are utilized as the unseen subsets for generalization capability evaluation.

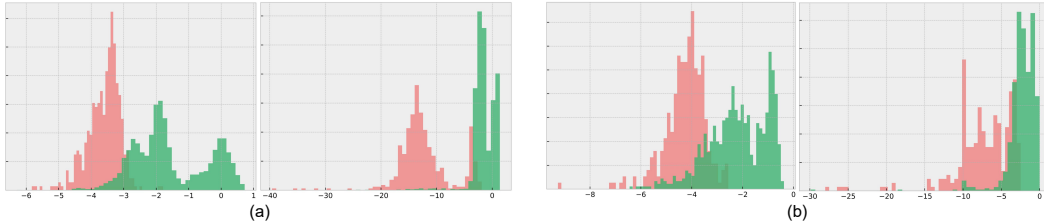


Figure 9: Log-likelihood histograms from (a) feature level 0 and (b) feature level 1. Left is the log-likelihood histogram w/o anomaly samples, right is the log-likelihood histogram with anomaly samples.

Table 7: Two hard subsets constructed from the MVTecAD dataset.

|          | First Subset |  | Second Subset |   |
|----------|--------------|--|---------------|---|
|          | Category     | Easy Anomaly Categories  | Category      | Hard Anomaly Categories                   |
| Textures | Carpet       | color, cut, hole, metal, contamination   | Carpet        | thread                                    |
|          | Grid         | broken, metal, contamination, thread   | Grid          | glue, bent                                |
|          | Leather      | color, fold, glue, poke  | Leather       | cut                                       |
|          | Tile         | crack, glue_strip, gray_stroke, oil  | Tile          | rough                                     |
|          | Wood         | color, combined, hole, liquid  | Wood          | scratch                                   |
| Objects  | Bottle       | broken_large, broken_small   | Bottle        | contamination                             |
|          | Cable        | bent_wire, combined, cut_inner_insulation, cut_outer_insulation, missing_cable | Cable         | cable_swap, missing_wire, poke_insulation |
|          | Capsule      | crack, squeeze   | Capsule       | faulty_imprint, poke, scratch             |
|          | Hazelnut     | crack, hole, print   | Hazelnut      | cut                                       |
|          | Metal nut    | bent, color, flip  | Metal nut     | scratch                                   |
|          | Pill         | color, combined, contamination, faulty_imprint, pill_type                      | Pill          | crack, scratch                            |
|          | Screw        | scratch_head, scratch_neck, thread_top   | Screw         | manipulated_front, thread_side            |
|          | Toothbrush   | defective  | Toothbrush    | defective                                 |
|          | Transistor   | bent_lead, cut_lead, misplaced   | Transistor    | damaged_case                              |
|          | Zipper       | broken_teeth, combined, fabric, border, rough, split_teeth                     | Zipper        | fabric_interior, squeezed_teeth           |
|          |              |  |               |   |
|          |              |  |               |   |